
This is an electronic reprint of the original article.
This reprint may differ from the original in pagination and typographic detail.

Mekgwe, Gadifele Nicolene; Akinwamide, Samuel Olukayode; Akinribide, Ojo Jeremiah; Olubambi, Peter Apata

Insight into tribological and corrosion behaviour of binderless TiC_xN_y ceramic composites processed via pulsed electric current sintering technique

Published in:
Ceramics International

DOI:
[10.1016/j.ceramint.2022.05.129](https://doi.org/10.1016/j.ceramint.2022.05.129)

Published: 01/09/2022

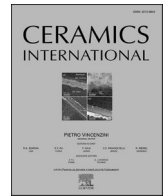
Document Version
Publisher's PDF, also known as Version of record

Published under the following license:
CC BY

Please cite the original version:

Mekgwe, G. N., Akinwamide, S. O., Akinribide, O. J., & Olubambi, P. A. (2022). Insight into tribological and corrosion behaviour of binderless TiC_xN_y ceramic composites processed via pulsed electric current sintering technique. *Ceramics International*, 48(17), 24793-24802. <https://doi.org/10.1016/j.ceramint.2022.05.129>

This material is protected by copyright and other intellectual property rights, and duplication or sale of all or part of any of the repository collections is not permitted, except that material may be duplicated by you for your research use or educational purposes in electronic or print form. You must obtain permission for any other use. Electronic or print copies may not be offered, whether for sale or otherwise to anyone who is not an authorised user.



Insight into tribological and corrosion behaviour of binderless TiC_xN_y ceramic composites processed via pulsed electric current sintering technique

Gadifele Nicolene Mekgwe^a, Samuel Olukayode Akinwamide^{a,b,*}, Ojo Jeremiah Akinribide^a, Peter Apata Olubambi^a

^a Centre for Nanomechanics and Tribocorrosion, School of Mining, Metallurgy and Chemical Engineering, University of Johannesburg, Doornfontein Campus, Johannesburg, South Africa

^b Advanced Manufacturing and Materials Research Group, Department of Mechanical Engineering, Aalto University, Espoo, Finland

ARTICLE INFO

Keywords:

TiCN cermets
Titanium nitride
Spark plasma sintering
Frictional coefficient
Electron backscattered diffraction
Potentiodynamic polarization

ABSTRACT

The study presents the corrosion behaviour and wear response of pulsed electric current sintered binderless $\text{TiC}_{50}\text{N}_{50}$, $\text{TiC}_{70}\text{N}_{30}$, and $\text{TiC}_{90}\text{N}_{10}$ based ceramic composites, consolidated by spark plasma sintering (SPS), and the relative densities were evaluated using the Archimedes principle. The microstructural evolutions of the sintered samples were examined through various microscopy techniques, and their susceptibility to corrosion in aggressive chloride environment was assessed using open circuit potential, potentiodynamic polarization and electrochemical impedance spectroscopy (EIS) methods. The microstructural examination of the specimens showed the presence of different phases within the titanium carbonitride (TiCN) cermets. The wear resistance evaluated using the frictional coefficient (COF) and calculated wear rate showed that the specimens exhibited an improved resistance. The specimens further showed enhanced resistance to corrosion in the test electrolyte, as the $\text{TiC}_{50}\text{N}_{50}$ cermet displayed enhanced resistance to the aggressive chloride ions in comparison to the other specimens.

1. Introduction

The significance of lowering production and maintenance costs in major engineering applications has enhanced the need to investigate and produce affordable advanced materials with improved mechanical properties. The fabrication of engineering components suitable for various emerging technological applications depends on these materials for secure and reliable operations. Materials such as TiCN based cermet has received enormous attention owing to their beneficial mechanical and physical properties, which include high hardness (2500–3000 HV), high melting temperatures (3050 °C), wear and improved corrosion resistance [1,2]. Moreover, Titanium carbide (TiC) and titanium nitride (TiN) possess FCC crystal structure and form a substantially complete solid solution where the stoichiometry ratio of carbon and nitrogen atoms in the form of TiC_xN_y (as $x + y = 1$) exhibits a wide range of composition [3,4]. Thus, numerous TiCN with respect to various compositions, stress states, and morphologies are employed for applications requiring enhanced toughness [5,6].

TiCN based cermets are also utilized in high-speed cutting processes and milling operations due to the lower frictional coefficient and improved oxidation resistance they exhibit compared to other conventional cermets. Tungsten carbide (WC) and TiCN based cermets are composites with ceramic and metal phases, whereby the metallic phase imparts toughness, while hardness is induced by the ceramics phase [7]. Several studies have been carried out on the enhancement of mechanical properties of cermets [8,9] through the incorporation of metallic binders such as Nickel (Ni), cobalt (Co), iron (Fe), molybdenum (Mo) [10–13], and various secondary carbides which include but not limited to tantalum carbide (TaC), hafnium carbide (HfC), niobium carbide (NbC), and molybdenum carbide (MoC) [14–17]. However, the addition of metallic binders causes mechanical and corrosion resistance deterioration compared to the matrix ceramic phase [18].

Several researchers have investigated the wear and corrosion behaviour of TiCN cermets. A recent study by Ren et al. [19] demonstrated the wear performance of TiCN cermets under different abrasives. The volume loss of TiCN was reportedly increased with increased sliding

* Corresponding author. Advanced Manufacturing and Materials Research Group, Department of Mechanical Engineering, Aalto University, Espoo, Finland.
E-mail addresses: samuel.akinwamide@aalto.fi, akinwamidekayode@gmail.com (S.O. Akinwamide).

<https://doi.org/10.1016/j.ceramint.2022.05.129>

Received 14 March 2022; Received in revised form 26 April 2022; Accepted 11 May 2022

Available online 18 May 2022

0272-8842/© 2022 The Authors. Published by Elsevier Ltd. This is an open access article under the CC BY license (<http://creativecommons.org/licenses/by/4.0/>).

distance. The study further showed that the hardness property of the TiCN cermet and abrasives plays a crucial role in determining the wear resistance of the cermet. Onuoha et al. [20] studied the effect of metallic binder and carbide on corrosion properties of steel reinforced cermets. The cermets fabricated via melt infiltration process reportedly exhibit increased corrosion resistance with reducing carbide content. This behaviour was ascribed to increased surface area covered by the oxide films formed from the dissolution of the metallic binder phase. Furthermore, the susceptibility of TiCN reinforced Ni cermet to corrosion in sulphuric acid was investigated by Chen et al. [21] with the cermets showing three passive zones. The first was enlarged with decreased current, while the rest were within the pseudopassive range. The EIS analysis revealed that the increased Cr content enhanced the impedance of the cermets. An increase in carbide content would improve the wear resistance.

Electrochemical aqueous corrosion studies have shown that the metallic binder phase influences the corrosion behaviour of the cermets owing to its selective dissolution, but the ceramic phase remains resistant [22,23]. To mitigate the challenges imposed by binders in hard materials, the concept of binderless cermets has been studied in corrosive environments [24]. Thus, a detailed examination of the wear and corrosion resistance of binderless cermet systems validates its relevance in the metal cutting industry. In this study, the wear and corrosion behaviour of binderless TiC_xN_y based ceramic composites was investigated.

2. Experimental procedure

2.1. Morphology and compaction of starting powders

Commercially available titanium carbonitride (TiC_xN_y) ceramic powders were used as the starting material in this study. The constitutional composition of the powders is listed in Table 1, while the SEM morphologies and XRD plot are presented in Fig. 1a-c and Fig. 2, respectively. The raw powder exhibits an irregular shape, with an agglomeration of relatively large particles. Also, the XRD plots for the powders show a uniform peak and distribution, with the dominant peaks represented at 2θ values of 25° , 36.2° , 43° , 63.1° , 74.7° and 82° . The decrease in the intensity of a major peak in the $\text{TiC}_{90}\text{N}_{10}$ powder is an indication that most of the peaks are dominated by TiC phases. The powders were poured into a graphite die with a diameter of 40 mm, followed by spark plasma sintering (model HHPD-25 from FCT system GmbH Germany) in a vacuum. The temperature was controlled by a pyrometer, and was used to determine the temperature of the sample through infrared radiation. The sintering temperature of 2100°C , heating rate of $100^\circ\text{C}/\text{min}$, 50 MPa pressure and 10 min holding time were maintained throughout the sintering process. The density of the sintered compacts was determined using the Archimedes principle.

2.2. Microstructural characterization

The specimens sectioned from the sintered compacts were prepared for microstructural analysis by preparation using the standard grinding and polishing metallographic procedures until a scratch-free and shiny surface was attained. Microstructural examination was carried out using a TESCAN Vega3 XMU scanning electron microscope (SEM) equipped

Table 1
Specification of the starting powders.

Sample	Average Particle size (μm)	Manufacturer	Theoretical Density (g/cm^3)
$\text{TiC}_{50}\text{N}_{50}$	1.5	H.C. Starck	5.08
$\text{TiC}_{70}\text{N}_{30}$	1.3	H.C. Starck	5.02
$\text{TiC}_{90}\text{N}_{10}$	1.4	Japan New Metals	4.96

with Energy Dispersed X-ray spectroscopy (EDS). Standard metallographic procedures were also adopted to prepare the specimens for electron backscattered diffraction (ESBD) scans, but a longer time was spent on final polishing to achieve good indexing. The images were obtained using a Zeiss Scanning electron microscope, equipped with a QUANTAX EBSD detector from Bruker. The X-ray diffraction (XRD) analysis was investigated using a W 1710 by Philip diffractometer equipped with copper target $K\alpha$ radiation at 20 mA and 40 kV. Prior to analysis, the specimens were sectioned to a dimension of $10\text{ mm} \times 5\text{ mm}$, after which the surfaces were ground to allow penetration and reflection of diffraction rays.

2.3. Tribology tests

The tribological behaviour of the TiC_xN_y sintered materials was studied under dry sliding conditions. $\text{TiC}_x\text{N}_y/\text{Al}_2\text{O}_3$ tribopairs were thoroughly cleaned and rinsed in ethanol. Tribology test was carried out on a standard tribometer (TRB tribometer, Anton Paar) using ball on disc configuration, according to ASTM G 133-95 standard. The alumina ball with a surface roughness of 15 nm was used as the counterface material. A load and linear speed of 10 N and 10 cm/s were respectively maintained throughout the test. Additional test parameters are presented in Table 2. The average frictional coefficient value was estimated, and the volumetric wear rate was calculated using equation (1) [25]. Post wear examination were conducted on the surface of the specimens using SEM to understand the wear mechanism.

$$W = \frac{m}{\rho \cdot P \cdot S} \quad (1)$$

where:

m = volume loss (g), W = Wear rate (mm^3/Nm), ρ = Density of the disk (g/mm^3), P = applied load (N), and S = sliding distance (m).

2.4. Corrosion tests

The corrosion resistance of the specimens was investigated in 3.5 wt % sodium chloride electrolyte at ambient temperature using a VerstaStat 4 potentiostat, operating on a VersaStudio 2.60.6 software. To ensure proper conductivity between the specimen and the potentiostat, a copper wire was attached to the base of the specimens. The surface of the specimens was prepared by grinding to 1200 grits of silicon carbide paper and polished using diamond suspension and fumed silica. Prior to potentiodynamic polarization, an open circuit potential test was conducted for 2 h to ensure adequate stabilization of the specimens in the test environment. Potentiodynamic polarization was conducted by scanning from an initial to final potentials of -1.5 V and 1.5 V respectively, at a scan rate of $0.2\text{ mV}/\text{s}$. The specimens were further analyzed using EIS technique to determine the charge transfer between the surface of the specimens and the test electrolyte at an initial and final frequency of 0.01 Hz and 100,000 Hz, respectively. The corrosion tests were repeated thrice to ensure reproducibility of the results.

3. Results and discussion

3.1. Densification behaviour

As determined by the Archimedes principle, the relative density of the sintered binderless cermets is shown in Fig. 3. With the sintering parameters adopted for fabrication, it is evident that the density of the TiCN ceramic composites increases linearly with increasing TiC content. All the sintered specimens achieved relative densities within 97.81–98.69%. Further observation showed that the relative densities increased with increasing TiC content, and the $\text{TiC}_{90}\text{N}_{10}$ specimen exhibited the highest density of 98.69%. The enhanced relative density of this specimen can be attributed to the absence of a metal binder phase

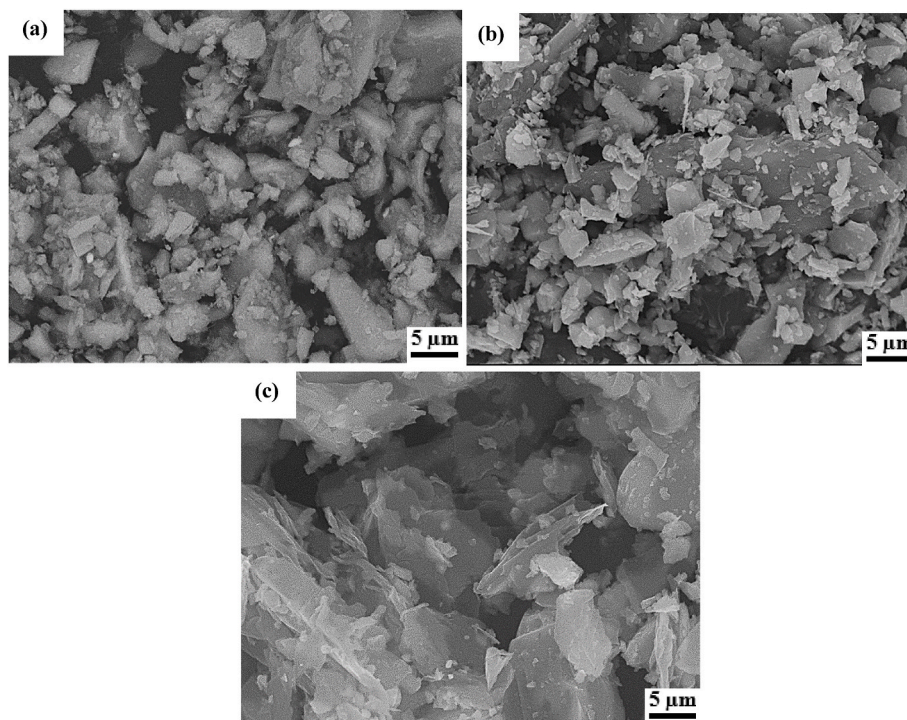


Fig. 1. SEM micrographs of (a) TiC₅₀N₅₀ (b) TiC₇₀N₃₀ (c) TiC₉₀N₁₀.

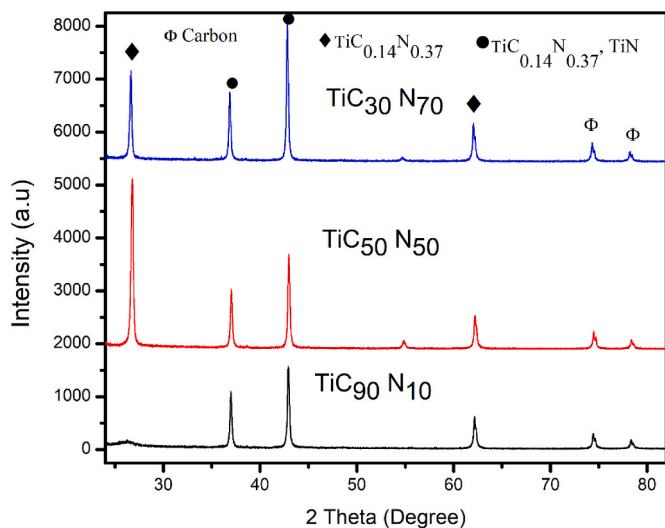


Fig. 2. XRD plot of the powders before sintering.

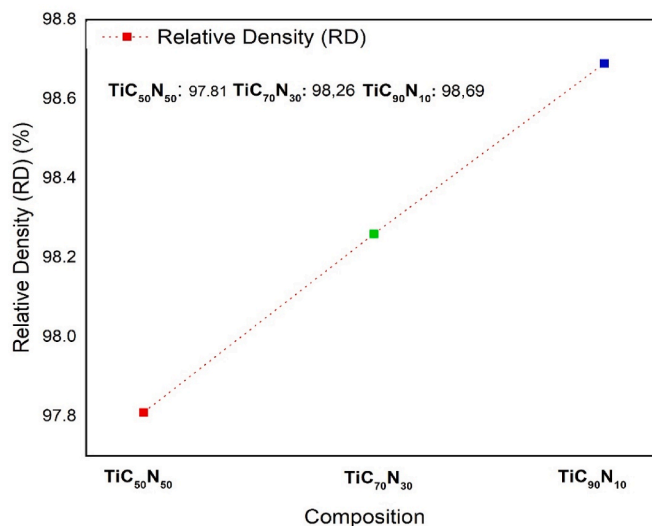


Fig. 3. Relative density of different TiCN compositions.

Table 2
Summary of the ball-on-disk test parameters.

Parameters	Value	Units
Acquisition rate	100	Hz
Linear speed	10	cm/s
Sliding distance	2000	m
Radius of wear track	6	mm
Humidity	50	%
Temperature	23 ± 2	°C
Load	10	N
Ball dimension	6	mm
Disk dimension	Φ 40 × 5	mm

[26]. A similar study on the effect of copper (Cu) addition on TiCN based cermet reported a decreased relative density with increasing Cu content. This behaviour was due to the introduction of Cu element, which generates pores, thus reducing the relative density since the densification process of cermet depends on the dissolution-precipitation [27]. The effect of metal binders on densification has been reported in the literature [28,29]. Poor wettability between the metal and ceramic phase often results in poor densification and decreased tribological and corrosion properties [30]. However, binders were not used in this present study, hence the reason for the excellent densification achieved. The density for TiC₅₀N₅₀ is marginally lower when compared to TiC₇₀N₃₀ and TiC₉₀N₁₀ compositions. This can be attributed to the TiC and N composition balance, as the latter is known for inducing porosities in composites [31]. A recent study by Yang et al. [32] reported an

improvement in the relative density of sintered compacts, and this enhancement was ascribed to the high sintering temperature adopted during fabrication. In comparison with other conventional fabricating techniques, SPS exhibits high relative densities due to its high efficiency in consolidating ceramic and metallic powders. Also, sintering at high temperatures increases the densification rate due to elemental diffusion and particle re-arrangement [33,34].

3.2. XRD analysis of sintered compacts

The XRD analysis of the sintered cermet is represented in Fig. 4 (a–c), and the binderless titanium carbonitrides specimens showed several remarkable peaks. The strength of the discovered peaks shows the presence of two different phases. According to Ilyasov et al. [35], TiCN exhibits two primary phases (TiC and TiN with unit cell diameters of 0.4311 nm and 0.3875 nm respectively). The FCC structure of $\text{TiC}_{50}\text{N}_{50}$ is traceable to sodium chloride type with Fm3m space group for TiCN phase, according to the characteristics of each of the phases. The FCC also indicates that carbon atom statistically fills the metal lattice and octahedral interstitial spaces compared to $\text{TiC}_{50}\text{N}_{50}$, which is attributed to space group number Pm3 m. Ti and N atoms occupy the octahedral interstitial site of the volume-centred cubic structures of $\text{TiC}_{70}\text{N}_{30}$ and $\text{TiC}_{90}\text{N}_{10}$ [36]. The reference unit cell was made up of sintered titanium carbide compact with a purity of 99.8%. The major phases and respective unit cell dimension of the specimens are presented in Table 3.

The phase molar concentration of titanium nitride in the TiCN composites under examination is indirectly influenced by the carbonitride (CN) phase, and it is consistent with the B1-type structure [39]. However, due to TiC and N's interaction, the excess Ti dissolves in the (CN), displacing the TiC composition stoichiometrically [39]. As a result, the emergence of TiCN and the Ti particle substitution by impurity atoms decreases the unit cell dimension of the TiC phase. It should also be noted that there is an appreciable increase in grain size after sintering, and there has been a discrepancy in the determining the accuracy of this increase through XRD and SEM analyses. The influence of the crystallite sizes and the effect of internal stress induced during sintering should be addressed for more accurate assessment of grain sizes.

Table 3

Dominant phases identified in the three sintered cermets.

Phase analysis of specimens	Structural mode	Space groups	Unit cell dimension (nm)	References
TiN	B1	Fm-3m	0.3875	[37]
TiC	B1	Fm-3m	0.4311	[38]
TiC_{70}	B1	Fm-3m	0.4330	[36,38]

3.3. Microstructure of sintered TiCN based ceramic composites

The SEM and EDS images of the sintered binderless TiCN ceramics are presented in Fig. 5. The different colour contrast (black and grey) seen in the micrographs, can be ascribed to the enrichment of various elements in the phases [40]. The microstructure of binderless TiCN has not been broadly explored due to the inexistence of numerous chemical and stoichiometric compositions of the cermet. Fig. 5a reveals a uniform microstructure with uniform grain size, owing to the presence of appreciable TiC content [41], which inhibits grain growth, thereby resulting in a fine-grained microstructure. A similar microstructure was reported in studies conducted by Russias et al. [42] and Chen et al. [43]. From Fig. 5b and c, the decreased TiC composition resulted in increased grain growth, which led to the formation of coarse grains. Furthermore, the increased nitrogen content promotes grain growth, which in turn reduces the solubility of TiCN solution. A similar observation was reported in a study by Shi et al. [44]. It should be noted that coarse grains might be generated through the initial agglomerates present in the powder source, thereby exhibiting completely recrystallized textures constituting bimodal grain distribution with different diameters [45]. Therefore, during the powder preparation process, de-agglomeration treatment such as ultrasonic conditioning should be considered [46]. A comparison between the specimens shows that the specimen with $\text{TiC}_{50}\text{N}_{50}$ composition exhibits a homogenous microstructure with fine grains, which will significantly enhance its mechanical properties, according to Hall-Petch theory [47,48]. The EDS of the images corroborates the stoichiometric distribution of the TiC and N composition in the cermets.

3.4. Electron backscattered diffraction analysis

The electron backscattered diffraction technique (EBSD) was

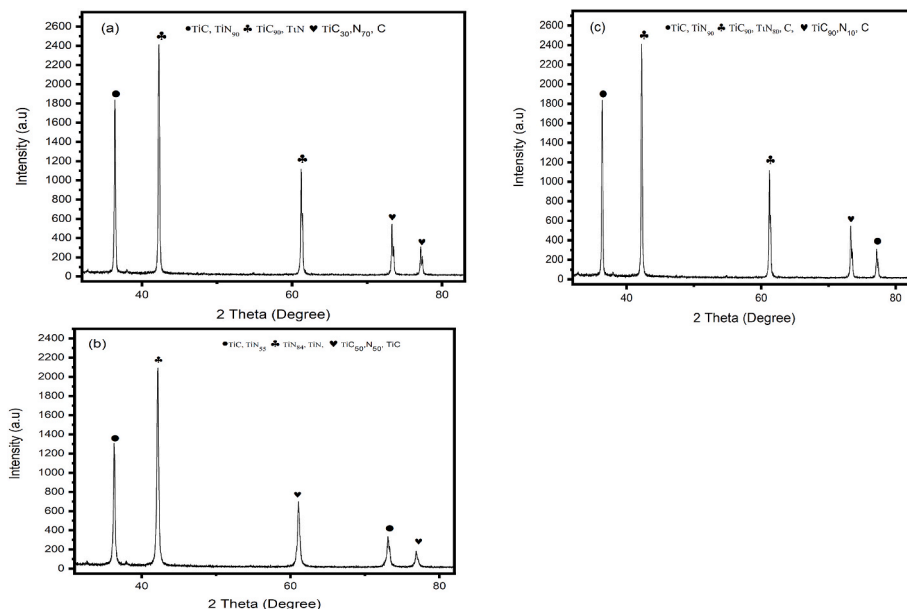


Fig. 4. XRD plots of (a) $\text{TiC}_{50}\text{N}_{50}$ (b) $\text{TiC}_{70}\text{N}_{30}$ (c) $\text{TiC}_{90}\text{N}_{10}$ cermet.

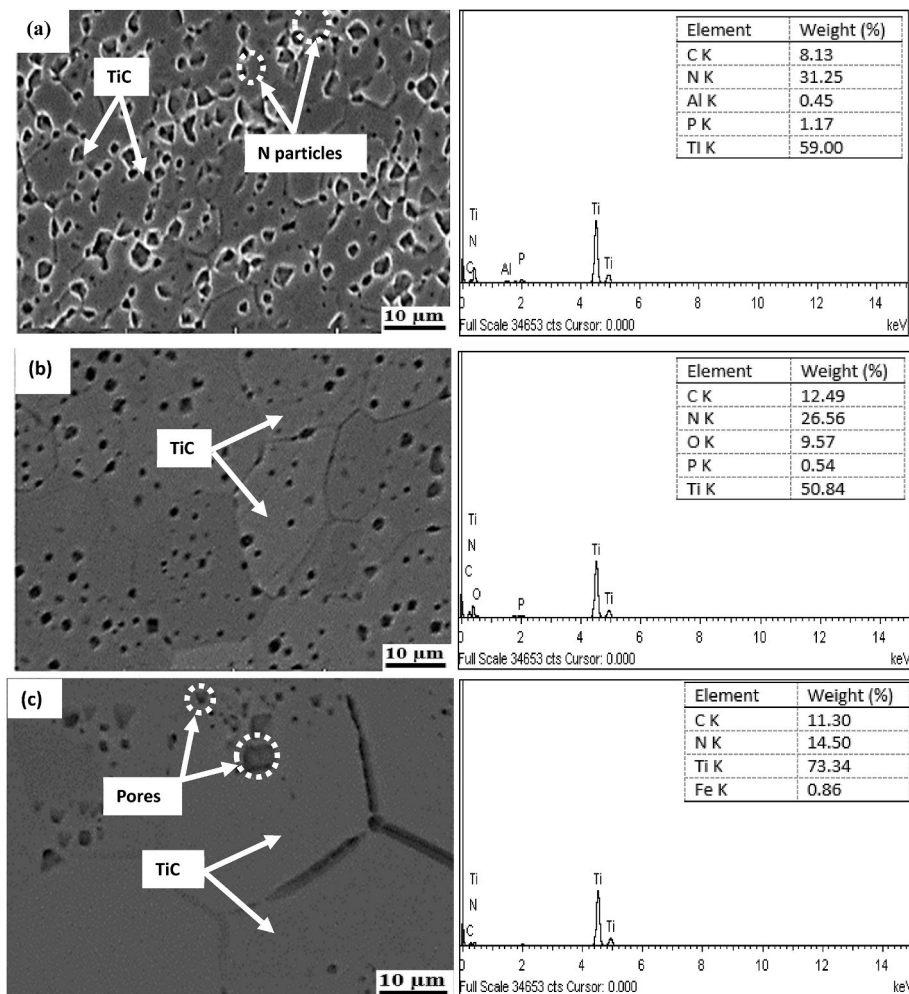


Fig. 5. SEM and EDS images of (a.) $\text{TiC}_{50}\text{N}_{50}$ (b) $\text{TiC}_{70}\text{N}_{30}$ (c) $\text{TiC}_{90}\text{N}_{10}$ cermets.

employed to identify and understand the crystallographic features of the specimens, and the inverse pole figure maps obtained are presented in Fig. 6. The maps displayed in Fig. 6a and b reveal two distinct regions: the alpha-rich colonies (dark region) and the carbon-rich phase (light region). Another grey region, made up of single alpha grains, is also evident in the microstructure. Close observation at Fig. 6c further reveals a beta-grain border, indicating minor plastic deformation and an alpha core rim structure with fewer Ti grains. The EBSD pattern of all the composites shows a reduced fine-grains core rim size due to the variation in the weight of the TiC and N particles. In the outer rim core interfaces, fewer TiN phases were seen after the diffusion of fine particles into larger or coarse particles, forming a bimodal structure as seen in the microstructures. The EBSD phase maps illustrate the effect of spark plasma sintering parameters adopted for fabrication on the final products by forming equiaxed alpha grains in the transformed beta matrix. It is also evident that the $\text{TiC}_{90}\text{N}_{10}$ specimen has more refined α and β -grains. The IPF texture presented in Fig. 6d shows polycrystallinity and texture randomness of grains in the $\text{TiC}_{30}\text{N}_{70}$ cermet.

3.5. Fractography

The SEM micrographs of the fractured surface of the sintered cermets are shown in Fig. 7. The presence of several voids and dimples, which depict heavy shear deformation, is evident across the micrographs. The similar fracture surface of TiCN based cermets with different Co/Ni binder compositions was studied by Wang et al. [49]. The presence of closed pores observed in the micrographs can be attributed to

low relative density is usually noted on pure TiCN based cermets which coincide with the results obtained in another study [50]. Porosity in binderless TiCN ceramics is associated with lower relative densities, which promotes the formation of cleavages in fractured surfaces. This agrees with a recent study by Kim et al. [51]. The micrograph displayed in Fig. 7a indicates that the specimen fractured from the propagation of multiple cracks. A ductile fracture zone and microvoids are evident in the micrographs. Fig. 7b also shows a dull fracture surface, depicting the absence of ductile failure, which characterizes a transgranular brittle fracture with the rapid spreading of cracks coupled with cleavage appearance and planar microcracks. Fig. 7c reveals a predominantly cleavage pattern with pores corresponding to the coarse grains and segregation of carbon within the grain boundary [52]. All the samples studied in this work illustrate the fact that the fractures originated from the micropores within the specimens. As discussed in previous sections, a strong relationship exists between the processing method and the overall properties of TiCN cermets.

3.6. Sliding wear behaviour of pure/binderless TiCN based ceramics

Several investigations on the wear performance of TiCN based cermets have been widely reported [53,54]. It is confirmed that TiCN with binder phases exhibits poor wear resistance and is more susceptible to chemical attacks when compared to the carbide and nitride phases in the cermets. Subsequently, there is limited reports on binderless TiCN ceramics, which are regarded as the evolution of structural materials which can be utilized in severe conditions. Fig. 8 shows the wear

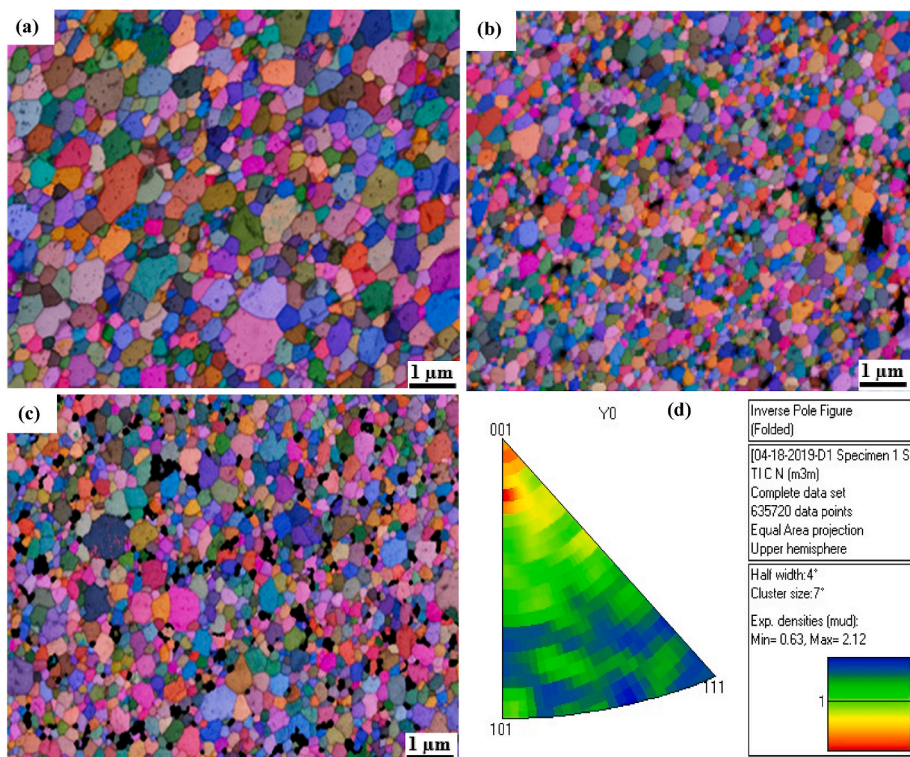


Fig. 6. EBSD inverse pole figure map for (a.) $\text{TiC}_{50}\text{N}_{50}$ (b) $\text{TiC}_{30}\text{N}_{70}$ (c) $\text{TiC}_{90}\text{N}_{10}$ and (d) inverse pole texture for $\text{TiC}_{30}\text{N}_{70}$ cermet.

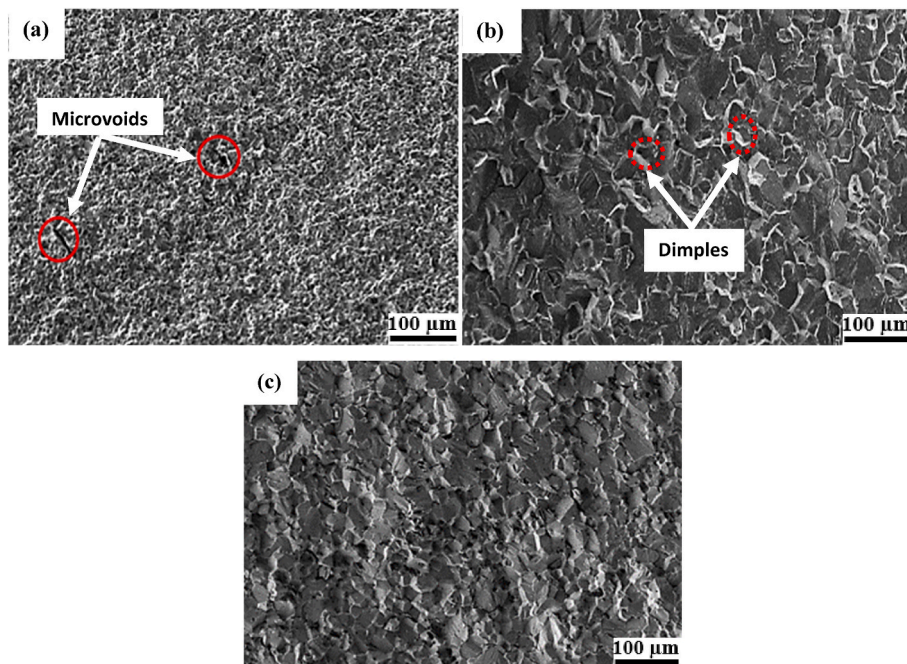


Fig. 7. Fracture morphology of sintered TiCN ceramics (a.) $\text{TiC}_{50}\text{N}_{50}$ (b) $\text{TiC}_{70}\text{N}_{30}$ (c) $\text{TiC}_{90}\text{N}_{10}$.

properties exhibited by the sintered cermets while sliding against alumina counterface at ambient temperature. Observation from the plots revealed the remarkable resistance of the specimens to deformation by wear, which makes the sintered binderless carbonitride specimens pertinent and suitable for the manufacture of high-speed cutting components. From Table 4, The specimen with $\text{TiC}_{50}\text{N}_{50}$ composition recorded a volume loss of 0.03 g, which is minimal compared to the surface degradation seen in the $\text{TiC}_{70}\text{N}_{30}$ and $\text{TiC}_{90}\text{N}_{10}$ cermets.

However, this behaviour can be ascribed to the uniform distribution and fine grains caused by the high TiN content, which inhibits further grain growth. Therefore, the higher mass loss of 0.06 g exhibited by the $\text{TiC}_{70}\text{N}_{30}$ and $\text{TiC}_{90}\text{N}_{10}$ specimens can be attributed to the presence of coarse TiCN grains, which intensified material removal due to abrasion between the two surfaces (counterface and specimen). Fig. 8a represents the plot of the average values generated from the frictional coefficient of the specimens. It is observed that the specimens recorded low frictional

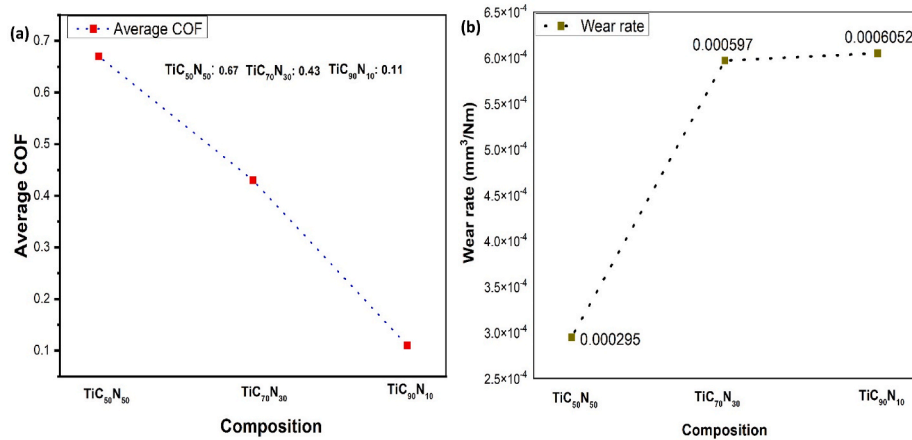


Fig. 8. Plots of (a) average frictional coefficient and (b) wear rate of TiCN cermets.

Table 4

Wear results of sintered binderless TiCN based ceramics at 10 N.

Specimen	Mass loss (g)	Wear rate (mm ³ /Nm)	Average COF
TiC ₅₀ N ₅₀	0.03	2.95×10^{-4}	0.67
TiC ₇₀ N ₃₀	0.06	5.97×10^{-4}	0.43
TiC ₉₀ N ₁₀	0.06	6.05×10^{-4}	0.11

coefficient, and this behaviour could be ascribed to a decrease in the rate at which the material layers are pulled from the sample surface due to lower frictional force and shear stress generated on the sample surface [25,55]. Further observation from Fig. 8b shows the plot of values obtained for the volumetric wear rate of the sintered ceramic composites as calculated using equation (1). It further reveals that the TiC₅₀N₅₀ specimen experienced high COF and low wear rate in comparison to the other specimens. The average COF values vary between 0.11 and 0.67, with TiC₅₀N₅₀ cermet exhibiting the highest value and TiC₉₀N₁₀ recording the least. To understand the dominant wear mechanism

responsible for removing the material layer from the surface of the specimens, a detailed analysis of the worn surfaces was investigated using SEM and EDS, and the morphologies observed are presented in Fig. 9(a–c). The micrograph of the TiC₅₀N₅₀ specimen revealed grain pull due to severe wear by abrasion. In addition, the grain pull-out is caused by debris ploughing from the surface of the cermet, which contributes to wear damage. The presence of oxygen in the EDS analysis of the worn ceramic surface showed the effect of heat generated between the counterface and the specimen, leading to the formation of oxide coatings on the specimen surface [56]. Additionally, high shear stresses at the contact interface are caused by a lack of tribo-layer formation and lubrication, leading to a rough track surface caused by continuous ploughing and chipping [57]. The EDS mapping of TiC₅₀N₅₀ cermet displayed in Fig. 10 shows the uniform distribution of the major elemental constituents of the specimen during the wear test.

3.7. Electrochemical analysis in 3.5 wt% NaCl

The open-circuit potential plots for the samples immersed in chloride

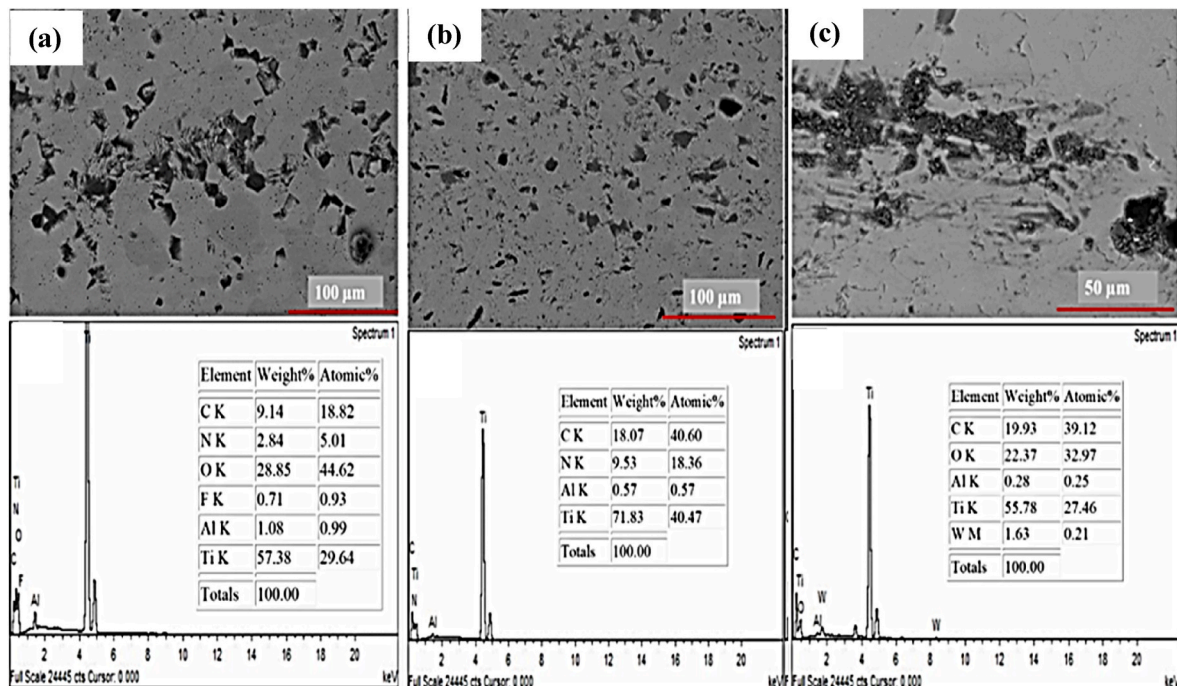


Fig. 9. BSE-SEM morphologies of worn sintered pure/binderless TiCN ceramics (A.) TiC₅₀N₅₀, (B) TiC₇₀N₃₀ and (C) TiC₉₀N₁₀.

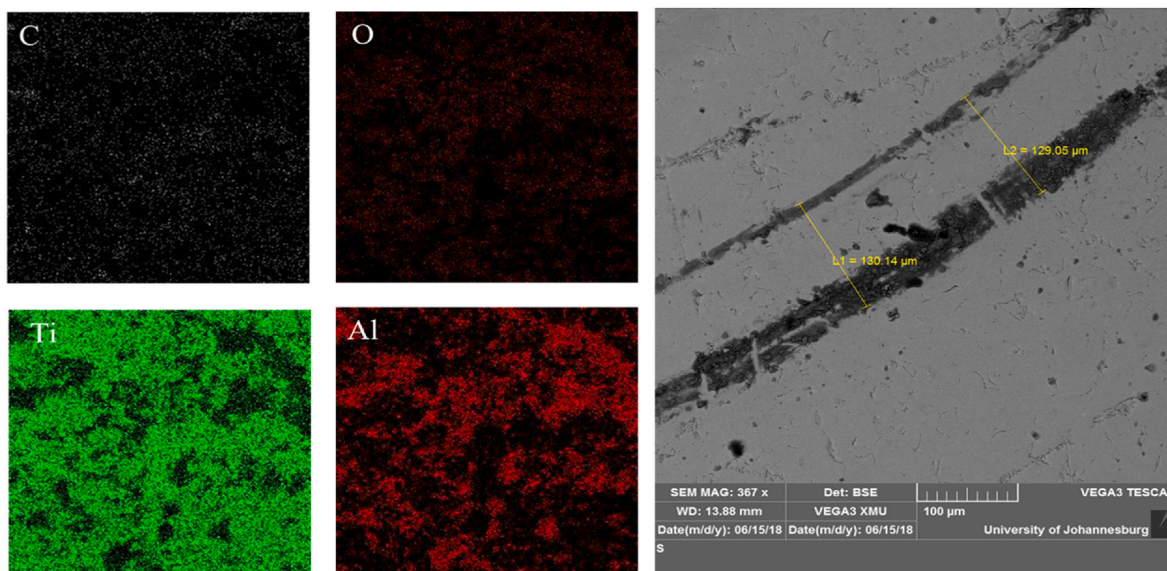


Fig. 10. EDS mapping of worn binderless TiCN based ceramic against Al_2O_3 ball at 10 N and wear track.

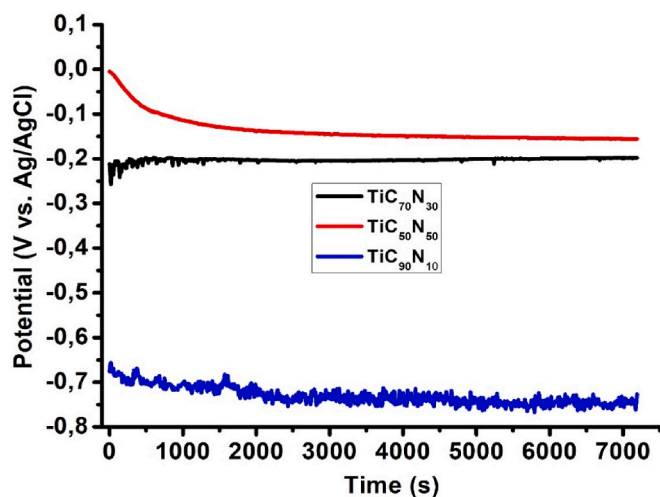


Fig. 11. Open circuit potential plot for specimens after 2 h immersion time in test electrolyte.

electrolyte are demonstrated in Fig. 11. Comparing the potentials of the cermets with respect to their nitride contents reveals that the specimen with the highest nitride content ($\text{TiC}_{50}\text{N}_{50}$) exhibited the highest open circuit potential, while the specimen with the least nitride addition ($\text{TiC}_{90}\text{N}_{10}$). However, a potential of 0.225 V was recorded in cermet with a nitride addition of 10%. The increased and noble electropositive potential observed in the cermet with composition ($\text{TiC}_{50}\text{N}_{50}$) depicts an enhanced resistance and rapid stability of the specimen to the aggressive chloride ions and electrolyte, respectively. The potentiodynamic polarization plots for the Ti(C, N) based cermet are presented in Fig. 10. All the curves are seen to display a potential passivation zone within the

Table 5

Electrochemical parameters from Tafel fitting of the potentiodynamic polarization curves.

Sample	E_{corr} (mV)	I_{corr} (μA)	Cathodic beta (mV)	Anodic beta (mV)
$\text{TiC}_{70}\text{N}_{30}$	-372.11	42.24	586.68	586.68
$\text{TiC}_{50}\text{N}_{50}$	-262.71	11.39	865.52	865.52
$\text{TiC}_{90}\text{N}_{10}$	-630.32	33.83	476.05	476.05

range of -0.5 V– 0.35 V vs Ag/AgCl to about 1.1 V– 1.4 V vs Ag/AgCl. The electrochemical characteristics parameters of the specimens presented in Table 5 are obtained by Tafel extrapolation of the anodic region of the polarization curves. The sample with $\text{TiC}_{70}\text{N}_{30}$ composition exhibited the highest current density, with a value of 42.24 μA , while the $\text{TiC}_{50}\text{N}_{50}$ specimen displayed the least current density with a value of 11.39 μA . It is noteworthy that the cermet with decreased current density will become less susceptible to chloride attack in the test electrolyte. Furthermore, Fig. 12 reveals a significant passivation region is seen to progress as the potential of the specimens tends toward the electropositive direction. However, the latter behaviour can be attributed to the possible formation of TiO_2 and a metal oxide binder phase. A similar observation was reported in a study by Kumar et al. [58]. It should also be noted that the current density and corrosion potential represent the specimens' kinetic and thermodynamic parameters, thereby predicting the corrosion behaviour of the material. Fig. 13a depicts the Nyquist impedance spectra of the specimens in 3.5% NaCl electrolyte. It further illustrates the resistance offered by the cermets when in contact with the aggressive chloride ions. The visible increase in the size of the

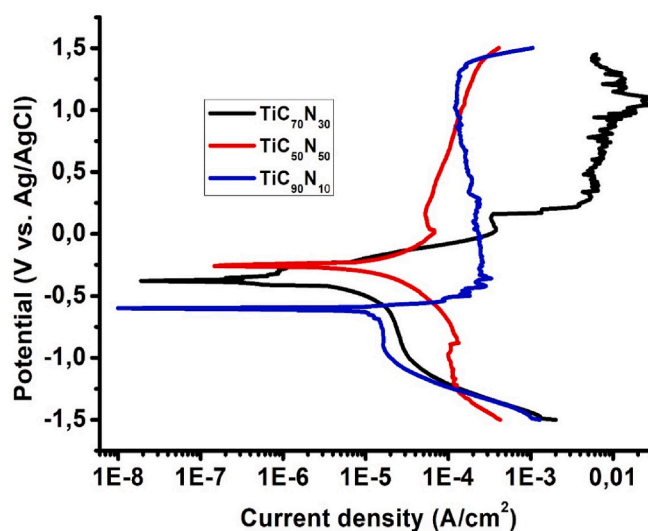


Fig. 12. Potentiodynamic polarization curves of the sintered cermets in 3.5 wt % NaCl.

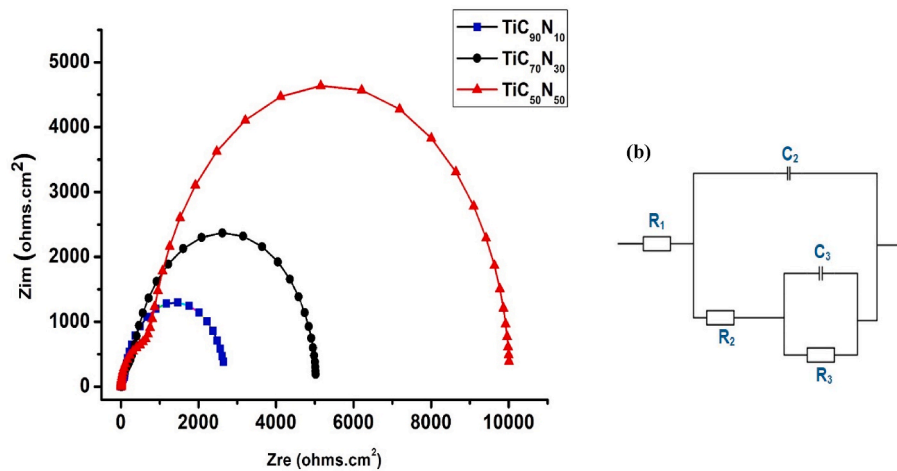


Fig. 13. (a) Nyquist EIS measurement plot of the sintered cermet in 3.5 wt% NaCl electrolyte and (b) equivalent circuit used for curve fitting.

semi-circle exhibited by the $\text{TiC}_{70}\text{N}_{30}$ and $\text{TiC}_{50}\text{N}_{50}$ specimens signifies enhancement in the passive film formed on the surface of the specimens with respect to an increase in nitrogen composition. This also confirms that nitrogen promotes the formation of passive resistant layers as it dissolves more into the binder. The electrochemical behaviour of the specimens is simulated using the equivalent circuit from the Z-fit simulator on an Ec-Lab electrochemical software. This circuit presented in Fig. 13b provides information on fitting parameters, which include charge transfer (C_3), film capacitance (C_2), transfer resistance (R_3), film resistance (R_2), and solution resistance (R_1) [59]. The values obtained from fitting these parameters are stated in Table 6. The highest charge transfer resistance of 856.3 Ω recorded by $\text{TiC}_{50}\text{N}_{50}$ indicates that it has the highest corrosion resistance in the aggressive chloride environment, while the least overall resistance (R_{sum}) of 2447 Ω seen in the $\text{TiC}_{70}\text{N}_{30}$ specimen depicts the fast dissolution of oxide layers formed on the surface of the specimen [60].

4. Conclusion

This study investigates the microstructural and tribological properties of spark plasma sintered TiCN cermet with varied stoichiometric ratio of TiC and N composition. The sintering parameters adopted for the cermet fabrication were further affirmed to yield enhanced relative densities between 97 and 99%. The high density was ascribed to the absence of a metallic binder phase in the cermet. The XRD analysis of the specimens revealed the presence of different phases of TiC and TiN within the TiCN cermet. At the same time, the SEM morphologies showed distinct contrast between the phases present. However, the reduced mass loss exhibited by the $\text{TiC}_{50}\text{N}_{50}$ cermet was ascribed to uniform distribution and fine grains caused by a balance between the TiC and TiN phases. The low frictional coefficient evident in the specimens was also attributed to a decrease in how materials are pulled from the surface of the specimens. Finally, the corrosion resistance of the cermet in 3.5 wt% presented $\text{TiC}_{30}\text{N}_{50}$ cermet as the most thermodynamically stable in the test electrolyte compared to other specimens. A similar observation was seen in the results obtained from EIS and potentiodynamic polarization analysis.

Table 6

EIS fitting parameters for specimens.

Sample	$R_1(\Omega)$	$R_2(\Omega)$	$R_3(\Omega)$	$C_1 (10^{-6}) \text{ F/cm}^2$	$C_3 (10^{-6}) \text{ F/cm}^2$	R_{sum}
$\text{TiC}_{70}\text{N}_{30}$	8.218	2693	319.8	240.07	30.03	3021.02
$\text{TiC}_{50}\text{N}_{50}$	15.64	5016	856.3	40.89	56.03	5887.94
$\text{TiC}_{90}\text{N}_{10}$	7.59	1016	1424	15.99	45.73	2447

Declaration of competing interest

The authors declare that they have no known competing financial interests or personal relationships that could have appeared to influence the work reported in this paper.

Acknowledgement

The authors are grateful to National Research Foundation of South Africa for funding this research.

References

- [1] P.K. Ajikumar, et al., Synthesis, characterization and evaluation of titanium carbonitride surface layers with varying concentrations of carbon and nitrogen, *Ceram. Int.* 38 (3) (2012) 2253–2259.
- [2] P.C. Siow, et al., Characterization of TiCN and TiCN/ZrN coatings for cutting tool application, *Ceram. Int.* 39 (2) (2013) 1293–1298.
- [3] O.J. Akinribide, et al., Studies on mechanical properties of graphite reinforced Ti (cx, N1-x) using nanoindentation techniques, *Procedia Manuf.* 30 (2019) 604–610.
- [4] Y. Peng, H. Miao, Z. Peng, Development of TiCN-based cermet: mechanical properties and wear mechanism, *Int. J. Refract. Metals Hard Mater.* 39 (2013) 78–89.
- [5] L. Karlsson, et al., Growth, microstructure, and mechanical properties of arc evaporated TiCxN_{1-x} ($0 \leq x \leq 1$) films, *Surf. Coating Technol.* 126 (1) (2000) 1–14.
- [6] O.J. Akinribide, et al., Microstructural and phase evolution of spark plasma sintering of graphitized Ti (C0. 9N0. 1) composites, *Int. J. Refract. Metals Hard Mater.* 78 (2019) 164–169.
- [7] T. Stewart, K. Plucknett, The sliding wear of TiC and Ti(C,N) cermet prepared with a stoichiometric Ni3Al binder, *Wear* 318 (2014) 153–167.
- [8] G.N. Mekgwe, et al., Fabrication of graphite reinforced TiCxNy by spark plasma sintering technique: a comparative assessment of microstructural integrity and nanoindentation properties, *Vacuum* 187 (2021), 110144.
- [9] P. Li, et al., Study on the formation of core–rim structure in Ti(CN)-based cermet, *Int. J. Refract. Metals Hard Mater.* 35 (2012) 27–31.
- [10] D. Dong, et al., Ti(C,N)-based cermet with fine grains and uniformly dispersed binders: effect of the Ni–Co based binders, *Ceram. Int.* 46 (5) (2020) 6300–6310.
- [11] L.W. Xu, et al., Effect of Ni contents on mechanical properties and corrosion behavior of Ti(C,N)-WC-Mo2C-(Ni,Co) cermet, *Mater. Chem. Phys.* 252 (2020), 123253.
- [12] B.V. Manoj Kumar, R. Balasubramaniam, B. Basu, Electrochemical behavior of TiCN–Ni-based cermet, *J. Am. Ceram. Soc.* 90 (1) (2007) 205–210.
- [13] E. Chicardi, et al., Toughening of complete solid solution cermet by graphite addition, *Chem. Eng. J.* 267 (2015) 297–305.
- [14] J. Wang, et al., The fabrication of multi-core structure cermet based on (Ti,W,Ta) CN and TiCN solid-solution powders, *Int. J. Refract. Metals Hard Mater.* 64 (2017) 294–300.
- [15] W. Wan, J. Xiong, M. Liang, Effects of secondary carbides on the microstructure, mechanical properties and erosive wear of Ti(C,N)-based cermet, *Ceram. Int.* 43 (1) (2017) 944–952. Part B.
- [16] W.T. Kwon, J.S. Park, S. Kang, Effect of group IV elements on the cutting characteristics of Ti(C,N) cermet tools and reliability analysis, *J. Mater. Process. Technol.* 166 (1) (2005) 9–14.
- [17] C. Park, S. Nam, S. Kang, Carbide/binder interfaces in Ti(CN)–(Ti,W)C/(Ti,W)CN-based cermet, *J. Alloys Compd.* 657 (2016) 671–677.

- [18] Y. Zheng, et al., Valence-electron structure and properties of main phases in Ti(C, N)-based cermets, *Mater. Chem. Phys.* 82 (3) (2003) 877–881.
- [19] X. Ren, et al., Abrasive wear behavior of TiCN cermets under water-based slurries with different abrasives, *Tribol. Int.* 66 (2013) 35–43.
- [20] C.C. Onuoha, et al., The effects of metal binder content and carbide grain size on the aqueous corrosion behaviour of TiC–316L stainless steel cermets, *Int. J. Refract. Metals Hard Mater.* 44 (2014) 129–141.
- [21] S. Chen, et al., Corrosion behavior of Ti (C, N)-Ni/Cr cermets in H₂SO₄ solution, *Int. J. Refract. Metals Hard Mater.* 47 (2014) 139–144.
- [22] L.-j. Wang, et al., Corrosion behavior of thermal sprayed WC cermet coatings containing metallic binders in saline environment, *Trans. Nonferrous Metals Soc. China* 23 (9) (2013) 2611–2617.
- [23] H. Rojacz, et al., High temperature corrosion studies of cermet particle reinforced NiCrBSi hardfacings, *Surf. Coating. Technol.* 222 (2013) 90–96.
- [24] H. Engqvist, et al., Microstructure and abrasive wear of binderless carbides, *J. Am. Ceram. Soc.* 83 (10) (2000) 2491–2496.
- [25] W. Ji, et al., Frictional behavior and wear resistance performance of gradient cermet composite tool materials sliding against hard materials, *Ceram. Int.* 43 (10) (2017) 7816–7826.
- [26] J. Qu, et al., Effect of WC content on the microstructure and mechanical properties of Ti (CO. 5N0. 5)-WC-Mo-Ni cermets, *Int. J. Refract. Metals Hard Mater.* 28 (2) (2010) 243–249.
- [27] L.W. Xu, et al., Effect of Cu addition on the microstructures and properties of ultrafine Ti(C,N)-based cermet, *Vacuum* 181 (2020), 109753.
- [28] S. Cardinal, et al., Microstructure and mechanical properties of TiC–TiN based cermets for tools application, *Int. J. Refract. Metals Hard Mater.* 27 (3) (2009) 521–527.
- [29] O.J. Akinribide, et al., Microstructural characterization and mechanical behaviours of TiN-graphite composites fabricated by spark plasma sintering, *Int. J. Refract. Metals Hard Mater.* 91 (2020), 105253.
- [30] B.M. Kumar, B. Basu, Mechanisms of material removal during high temperature fretting of TiCN–Ni based cermets, *Int. J. Refract. Metals Hard Mater.* 26 (6) (2008) 504–513.
- [31] Q. Yang, et al., Hardness and elastic properties of Ti(C_xN_{1–x}), Zr(C_xN_{1–x}) and Hf(C_xN_{1–x}), *J. Alloys Compd.* 309 (1) (2000) L5–L9.
- [32] X. Kang, et al., A study of the preparation and properties of dense binderless titanium carbonitride-based ceramics, *J. Alloys Compd.* 843 (2020), 155941.
- [33] B.-C. Kim, et al., Densification of nanocrystalline ITO powders in fast firing: effect of specimen mass and sintering atmosphere, *Mater. Res. Bull.* 40 (2) (2005) 395–404.
- [34] O. Akinribide, et al., Sintering of binderless TiN and TiCN-based cermet for toughness applications: processing techniques and mechanical properties: a review, *Ceram. Int.* 45 (17) (2019) 21077–21090.
- [35] V. Ilyasov, et al., X-ray diffraction study of the dependence of the fine TiC structure on dispersion of hardening phase particles, *Acta Metall. Mater.* 43 (5) (1995) 2115–2119.
- [36] A.N. Kovalenko, et al., Personalized energy systems based on nanostructured materials, *Наносистемы: физика, химия, Математика* 12 (3) (2021) 368–403.
- [37] H. Sharififard, M. Ghorbanpour, S. Hosseinirad, Cadmium removal from wastewater using nano-clay/TiO₂ composite: kinetics, equilibrium and thermodynamic study, *Advances in Environmental Technology* 4 (4) (2018) 203–209.
- [38] C. Musa, et al., Spark plasma sintering of self-propagating high-temperature synthesized TiC_{0.7}/TiB₂ powders and detailed characterization of dense product, *Ceram. Int.* 35 (7) (2009) 2587–2599.
- [39] M. De Cuyper, J.W. Bulte, *Physics and Chemistry Basis of Biotechnology*, vol. 7, Springer Science & Business Media, 2001.
- [40] J. Liu, et al., Mo element-induced wear behavior evolution of self-lubricant Ti(C, N)-based cermets, *Int. J. Refract. Metals Hard Mater.* 80 (2019).
- [41] H. Yang, et al., The enhanced superplasticity of a 2024 matrix nanocomposite reinforced by TiC particles, *Mater. Sci. Eng., A* 774 (2020), 138926.
- [42] J. Russias, et al., Influence of titanium nitride addition on the microstructure and mechanical properties of TiC-based cermets, *Int. J. Refract. Metals Hard Mater.* 23 (4) (2005) 358–362.
- [43] L. Chen, W. Lengauer, K. Dreyer, Advances in modern nitrogen-containing hardmetals and cermets, *Int. J. Refract. Metals Hard Mater.* 18 (2) (2000) 153–161.
- [44] Z. Shi, et al., Effect of nitrogen content on microstructures and mechanical properties of Ti(C, N)-based cermets, *J. Alloys Compd.* 568 (2013) 68–72.
- [45] O. Akinribide, et al., Mechano-chemical synthesis and characterization of Ti (C, N)-powder from TiN-MWCNTs/graphite, *Part. Sci. Technol.* 38 (8) (2020) 952–962.
- [46] P. Angerer, et al., Spark-plasma-sintering (SPS) of nanostructured titanium carbonitride powders, *J. Eur. Ceram. Soc.* 25 (11) (2005) 1919–1927.
- [47] P. He, et al., Elevated temperature mechanical properties of TiCN reinforced AlSi10Mg fabricated by laser powder bed fusion additive manufacturing, *Mater. Sci. Eng., A* 811 (2021), 141025.
- [48] Q. Li, et al., Insight into solidification microstructure control by trace TiCN–TiB₂ particles for yielding fine-tuned nanoprecipitates in a hypoeutectic Al–Si–Mg alloy, *Mater. Sci. Eng., A* 827 (2021), 142093.
- [49] Y. Wang, et al., Ti (C, N)-based cermets sintered under high pressure, *Int. J. Refract. Metals Hard Mater.* 54 (2016) 203–209.
- [50] G. Liu, et al., Spark plasma sintering of pure TiCN: densification mechanism, grain growth and mechanical properties, *Int. J. Refract. Metals Hard Mater.* 66 (2017) 68–75.
- [51] W. Kim, et al., High-frequency induction heated sintering of High-energy ball milled TiC_{0.5}N_{0.5} powders and mechanical properties of the sintered products, *Ceram. Int.* 39 (1) (2013) 585–591.
- [52] H. Xiong, et al., Ti(C,N)-based cermets containing uniformly dispersed ultrafine rimless grains: effect of VC additions on the microstructure and mechanical properties, *Ceram. Int.* 46 (12) (2020) 19904–19911.
- [53] G. Xian, et al., Mechanical and wear properties of TiN films on differently pretreated TiCN-based cermets, *Appl. Surf. Sci.* 570 (2021), 151180.
- [54] Z. Li, et al., Microstructure and properties of Ti (C, N)-TiB₂-FeCoCrNiAl high-entropy alloys composite cermets, *Mater. Sci. Eng., A* 767 (2019), 138427.
- [55] N. Lin, et al., Improvement in densification process and properties of Ti(C,N)-based cermets with vanadium carbide addition, *Ceram. Int.* 45 (2) (2019) 2692–2700. Part A.
- [56] A. Das, et al., Hard turning of AISI D6 steel with recently developed HSN2-TiAlxN and conventional TiCN coated carbide tools: comparative machinability investigation and sustainability assessment, *J. Braz. Soc. Mech. Sci. Eng.* 44 (4) (2022) 1–25.
- [57] J. Liu, et al., Formation of self-lubricant surface layer on the Ti(C, N)-based cermets, *Vacuum* 143 (2017) 225–228.
- [58] B.V. Manoj Kumar, R. Balasubramaniam, B. Basu, Electrochemical behavior of TiCN?Ni-based cermets, *J. Am. Ceram. Soc.* 90 (1) (2007) 205–210.
- [59] T.S. Tshphe, et al., Structural characterization and biocorrosion behaviour of direct metal laser sintered Ti6Al4V–ZrO₂ tracks: influence of processing parameters, *Results in Materials* 13 (2022), 100257.
- [60] L. Xu, et al., Effect of Ni contents on mechanical properties and corrosion behavior of Ti (C, N)-WC-Mo₂C-(Ni, Co) cermets, *Mater. Chem. Phys.* 252 (2020), 123253.